Effect of layer addition on residual stresses of wire arc additive manufactured stainless steel specimens

Sébastien Rouquette, Camille Cambon, Issam Bendaoud, Sandra Cabeza, Fabien Soulié

▶ **To cite this version:**

Sébastien Rouquette, Camille Cambon, Issam Bendaoud, Sandra Cabeza, Fabien Soulié. Effect of layer addition on residual stresses of wire arc additive manufactured stainless steel specimens. Journal of Manufacturing Science and Engineering, 2023, pp.1-12. 10.1115/1.4063446 . hal-04416636

HAL Id: hal-04416636
https://hal.science/hal-04416636

Submitted on 25 Jan 2024

HAL is a multi-disciplinary open access archive for the deposit and dissemination of scientific research documents, whether they are published or not. The documents may come from teaching and research institutions in France or abroad, or from public or private research centers.

L'archive ouverte pluridisciplinaire **HAL**, est destinée au dépôt et à la diffusion de documents scientifiques de niveau recherche, publiés ou non, émanant des établissements d'enseignement et de recherche français ou étrangers, des laboratoires publics ou privés.

Effect of layer addition on residual stresses of wire arc additive manufactured stainless steel specimens

Sébastien Rouquette*
Associate Professor
LMGC, Univ. Montpellier, CNRS
Montpellier, France

Camille Cambon
PhD
LMGC, Univ. Montpellier, CNRS
Montpellier, France

Issam Bendaoud
Associate Professor
LMGC, Univ. Montpellier, CNRS
Montpellier, France

Sandra Cabeza
ILL Scientist
Institut Max von Laue - Paul Langevin
Grenoble F-38042
France

Fabien Soulié
Professor
LMGC, Univ. Montpellier, CNRS
Montpellier, France

ABSTRACT

Residual stresses have been characterized in four Wire Arc Additive Manufacturing specimens with neutron diffraction technique. Firstly, two methods are investigated for obtaining the reference diffracted angle θ_0 that is required for the computation of micro-strains and, thus, the stresses. θ_0 was obtained with two approaches. The first one required a strain-free specimen in order to get directly the reference diffracted angles θ_0 in the three principal directions. The second one is based on the plane stress assumption to get θ_0 indirectly by imposing that the normal stress was equal to zero. Both methods led to similar residual stresses for the 1-layer specimen what validated this approach for all specimens without a strain-free specimen available. The second part of this work focused on the modification of the residual stresses in the specimen following the addition of a new deposit. The neutron diffraction measurements showed that the longitudinal stress was tensile in the heat affected and fusion zones with a maximum value located at the parent material - layers interface where the thermal loadings were applied. A decrease of this maximum value from 257 MPa to 199 MPa appeared after deposition of a new layer which is due to some stress relaxation effect. Inside the parent material, a large zone presents compressive longitudinal stress up to -170 MPa. The bottom part of the parent material is under tensile stress likely due to its upward bending following the thermal contraction of the deposited layers during cooling to ambient temperature.

Keywords: Wire Arc Additive Manufacturing, Residual Stresses, Neutron Diffraction, Stainless Steel 316L.

Nomenclature

U Welding voltage in Volt
I Welding current in Ampere
V Welding speed in meter per second
Ws Wire feed rate in meter per minute

*Address all correspondence to sebastien.rouquette@umontpellier.fr

λ Wavelength of neutron beam
hkl Miller indices
d_{hkl} Crystal lattice spacing
θ_{hkl} Measured scattering angle
ε_i Measured principal strains
σ_i Measured principal stresses
ν Poisson's ratio
E Young's Modulus

1 Introduction

Additive manufacturing (AM) techniques are based on layer-by-layer stacking of molten material with the assistance of Computer-Aided Design (CAD) model in the aim to develop three dimensional parts [1]. Compared with traditional manufacturing, Additive Manufacturing have the ability to produce complex components [1, 2]. Furthermore the material wastage for machining operations is estimated to be about 90% while it is about 20 % for AM operations [3]. The AM technique under interest in this work uses a arc welding source with a metallic filler wire. This technique is called Wire Arc Additive Manufacturing (WAAM). This process uses the heating generated by the electric arc to melt the filler wire that is deposited firstly on a substrate. A first deposit is then obtained on the substrate. Then another layer is deposited on the top of the former. The AM part is built by stacking the layers. The WAAM allows building parts up to few meters with relatively low forming costs and high manufacturing efficiencies [4].

However, issues such as large surface roughness, anisotropy of the microstructure, high hardness, high residual stresses prevent a fast industrial diffusion of WAAM process. Ding et al. discussed the effect of residual stresses and distortions on WAAM parts [5]. The distortions led to poor build tolerances, while the residual stresses negatively affected mechanical properties of the built part. Residual stresses are primarily caused by the compressive yielding that occurs around the melted zone as the material heats and expands under electric arc heating. During solidification, this zone contracts restraint by the surrounding solid material that causes tensile residual stresses. The tensile residual stresses reduce the fatigue strength and the toughness [6].

Understanding the generation of residual stresses during the WAAM operation is of high interest because it affects the structure integrity. One technique to measure the residual stresses inside metallic part is the neutron diffraction technique (ND). ND is a non-destructive technique that provides insights into strain and stress fields deeper inside the structures [7]. A description of strain and stress measurements using neutron and synchrotron radiation is given in [8]. The stress is deduced from the strain measurements by applying Hooke's law.

The residual stresses in the 1-layer specimen was computed using two approaches. Computation of the strains requires the reference diffracted angles θ_0 in the three principal directions. θ_0 was obtained either from the strain-free 1-layer specimen or indirectly by applying plane stress condition on normal direction. A strain-free specimen was only available for the 1-layer specimen. No strain-free specimens were available for the specimens with 2, 3 and 5 layers before carrying out the neutron measurements. The two approaches used to get the reference diffracted angle θ_0 are compared for the 1-layer specimen in order to validate the plane stress method. The second approach was used for the computation of the stresses in the 2-, 3- and 5-layers specimens. Then, the residual stress profiles inside the 4 specimens are presented and the effect of layer addition is discussed.

2 Experimental set-up, thermal history and micro-structure

2.1 Geometry and operating conditions

A schematic representation of the specimen is reported in Figure 1 and a photography of the 1-layer specimen is presented in Figure 2. The parent material is made of stainless steel 304L and the dimensions are 149 x 100/53 x 6 mm^3. The filler wire is made of stainless steel 316L and its diameter is 1 mm. During the deposition procedure, the parent material is clamped on the left side (the striped area). The other extremity is free to move. Up to 5 layers are stacked vertically as depicted in Figure 1.

A Gas Metal Arc Welding generator was used to melt the filler wire. The transfer of metal droplet was made under Cold Metal Transfer (CMT) which allowed the use of low welding energies with a high control of deposition rate. The layers are deposited on the edge and along the length of parent material as depicted in Figure 1. The process parameters including voltage, current, welding speed and shielding gas are reported in Table 1. The first layer of the specimen has been done with higher energy in order to lower the sink effect of the parent material and to promote a better wetting of the first layer. The 1-layer specimen has been manufactured twice. Then, five specimens : two 1-layer, one 2-layers, one 3-layers and one 5-layers were built with similar linear welding energy. One of the two 1-layer specimens has been cut off with water jet cutting machine in order to get a strain-free specimen. The cut was performed along the vertical line called V55 in Figure 1. This

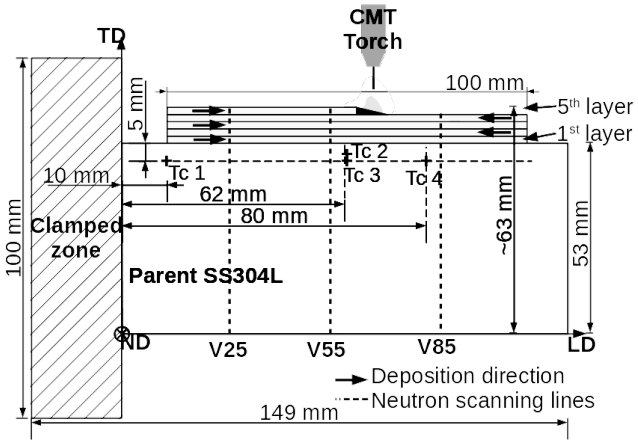

Fig. 1. Geometry of the specimen. The abbreviation Tc is for thermocouple and V25 means Vertical line at position 25 mm on the longitudinal direction (LD). The dash dotted lines (V25, V55 and V85) are the lines used for the neutron diffraction measurements. The deposited layers are schematized below the CMT Torch. The arrow in each layer shows the starting point and direction of deposition.

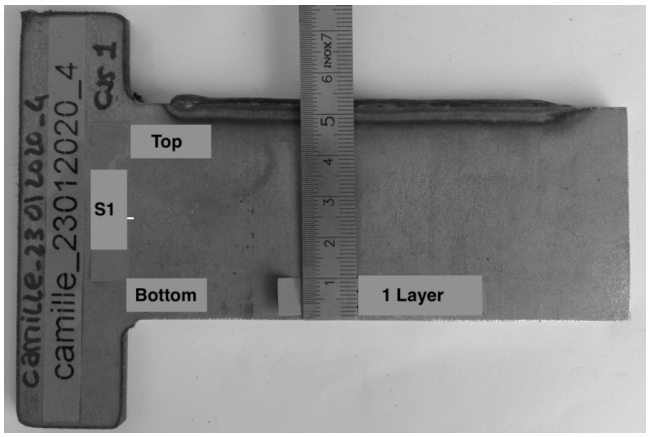

Fig. 2. Specimen with 1-layer. The deposited layer was done on the top edge of the parent material. A black oxidised zone, located between 50 and 55 mm, shows the zone of deposition. The starting point of the layer was on the left side, close to the word ”top” and the deposition direction was toward the right.

Table 1. Deposition parameters used for the elaboration of the four specimens. A mixture of 98 % Argon with 2 % Carbon Dioxide (CO_2) was employed as shielding gas.

Parameter	U (V)	I (A)	V (mm/s)	Ws (m/mn)	Shielding gas (l/mn)
1^{st} layer	13.4	123	7	4.2	15
layer 2 to 5	13.3	110	7	3.3	15

specimen has been used to measure the reference diffracted angles θ_0 in the three principal directions. The remaining part of the cut off specimen has been analyzed with EBSD technique in order to characterize the micro-structure of the melted zone.

The 5-layers specimen was thermally monitored with K-type thermocouples of 0.5 mm diameter from the first thermal cycle to the fifth one until it reached the ambient temperature of the laboratory.

2.2 Thermal history of the 5-layers specimen

The 5-layers specimen was monitored in-situ with 5 thermocouples (type K) located inside the parent material through holes of 1 mm diameter with a depth of 2 mm. The position of the thermocouples are displayed in Figure 1. Tc2 was located 3 mm below the deposition surface while the 4 others were located 5 mm below. Tc5 faced Tc3 but it was positioned on the opposite side of the parent material. The time evolution of the temperature for the 5 thermocouples is reported in Figure 3.

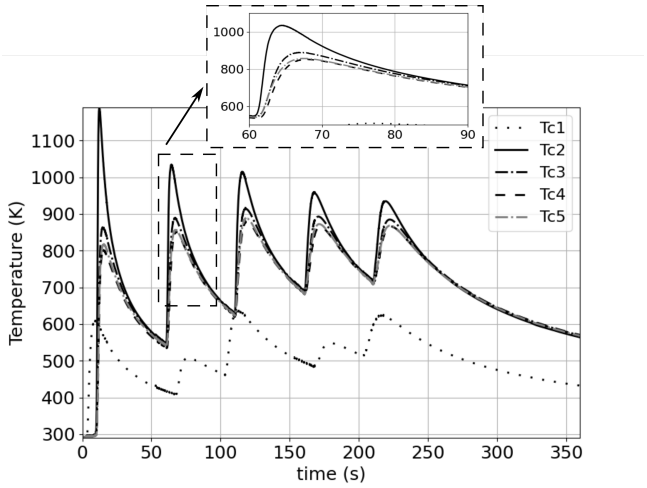

Fig. 3. Time evolution of the temperature measured during the deposition of the 5-layers specimen at the 5 thermocouples. An enlargement of the second thermal cycle is displayed on the top of the figure. Thermocouples 3, 4 and 5 did not exhibit large differences as they are located 5 mm below the top surface. This trend confirms that the thermal steady state is reached.

The 5 series of heating and cooling due to the 5 deposition cycles are clearly visible. The 5 thermocouples reached the ambient temperature after 1800 s as reported in Table 2. Tc1 presented the lowest temperatures as it was the farthest from the deposition area. Furthermore, it exhibited its highest values during the deposition of layers 1, 3 and 5 as it is close to the starting point of each odd layer. The layers were deposited such as the ending point of the 1^{st} layer was the starting one of the 2^{nd} layer and so on. This deposition strategy stabilized the height and width of stacked layers. An interlayer time of 35 s was imposed between each deposited layer.

Table 2. Evolution of the temperature (in Kelvin) as a function of time for thermocouples Tc2 and Tc3 until 1800s.

Thermocouple	12.5 s	64.5 s	115.5 s	168 s	220 s	250 s	400 s	600 s	800 s	1200 s	1800 s
Tc2 (K)	1189	1034	1013	958	934	773	532	444	397	346.8	316.8
Tc3 (K)	747	843	886	882	879	774	536	447	398.4	347.6	317.1

Thermocouples 3, 4 and 5 are localized in the thermal steady state zone because the measured temperatures are quite similar. Their maximum temperature was reached during the deposition of the 3^{rd} layer. Then these temperatures decreased slowly as each new layer addition resulted in a 2 mm height layer. So it has increased the distance between the thermal loading zone and the thermocouples what enhanced the heat loss by convection and radiation. Tc2 was located 3 mm below the deposition surface, that is why it recorded the highest temperature of about 1200 K during the deposition cycle 1. Then this maximum value decreased steadily after deposition cycles 2 to 5 as the surface of convection and radiation increased and so the heat loss. It can be seen that the initial temperature of all thermocouples (before each deposition) increased strongly after the 1^{st} layer and stabilized after the cooling of the 3^{rd} layer above 700 K.

2.3 Texture analysis

The texture analysis has been investigated by electron back scattered diffraction (EBSD) in order to characterize the size of the grains and the crystallographic orientation of the micro-structure of both parent material and deposited material. The two samples were taken close to the section V55, see Figure 1. The specimens were ground, then polished to a 1 micron finish with colloidal silica on a vibrating polishing machine. A Camscan Crystal Probe X500FE Scanning Electron Microscope (SEM) was used for carrying out this EBSD analysis. The data have been acquired with Aztec software and EBSD measurements were processed with Channel 5 software (both software are from Oxford instrument). The EBSD scan

was carried out using 3 μm step size with field width and height of 13.1 mm by 5.2 mm. The accelerating voltage was set to 20 kV and the number of collected points was around 7.59 x 10^6.

Figure 4 presents the EBSD orientation mapping for the 1-layer (top-left) and 5-layers (right) specimens. It is clearly visible in Figure 4 that the growth direction of columnar grains is in the direction of addition of the layers also labelled transverse direction (TD) as defined in Figure 1. This was expected because the deposits are made on the slice of the parent material what promoted the orientation of dendrites (in the opposed direction to the heat flow). It is well known that as molten metal cools, solidification occurs with the emergence and growth of dendrites, growing in the opposite direction to the heat flow. WAAM metallic parts often result in a columnar grain structure, leading to a highly textured material with anisotropic material properties [9]. An epitaxial grain zone is visible in the middle of the 1-layer specimen as well as in the 1^{st} layer of the 5-layers specimen. The low thermal gradient in this zone promoted this grain growth. The grain size has also been measured from Figure 4: about 10-15 μm in the parent material to few millimeters in the deposited layers. These highly textured zones are often the cause of poor neutron diffraction signals.

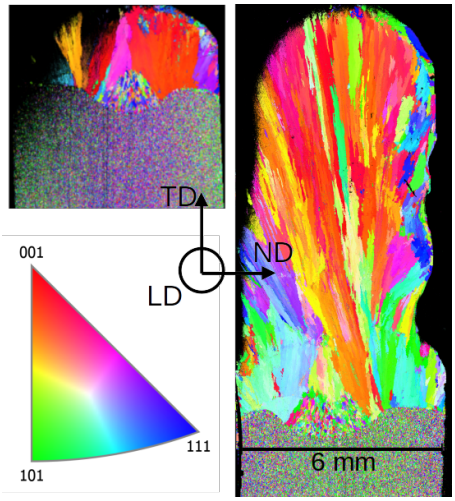

Fig. 4. EBSD orientation mapping in the longitudinal direction (LD) of specimens with 1 layer (top - left) and 5 layers (right). The two cross-sections were removed from twin specimens at position V55 of Figure 1.

In the deposited zone, the EBSD orientation mapping shows that there is no preferred orientation of the grains in the two first deposits (bottom half zone of deposits). Conversely, the family crystal plane $\{100\}$ is promoted in the two last deposits (top half zone of deposits) as it can be seen in Figure 4. This is confirmed with the pole figures displayed in Figure 6. These pole figures have been realised in the two last deposited layers. These pole figures show significant texture. The $\{100\}$ pole figure shows clearly high intensity spots in the three principal directions, representing up to 10.4 multiples of a uniform distribution (MUD). As a consequence of the significant texture in the deposited zone, the neutron measurements should be carefully interpreted. In contrast, the pole figures realised in the parent material suggest that it is lowly textured, see Figure 5. Although the $\{100\}$, $\{110\}$ and $\{111\}$ pole figures show some high intensity spots, the MUD is only 2.08. This value suggests that modest texture is present in the parent material.

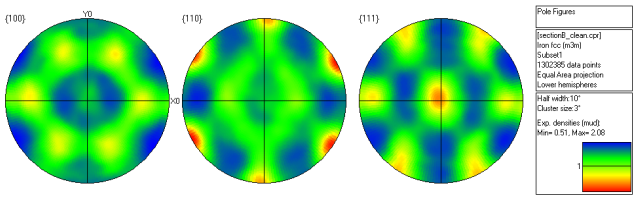

Fig. 5. Pole figures of parent material investigated by EBSD technique. The investigated zone is located below the fusion line.

The chemical composition in both the parent material and melted material has been carried out on the 5-layers specimen only. Two zones have been analyzed one in the parent material and the second one in the 3^{rd} layer. This analysis confirmed that the parent material was in SS304L with 70.4 % of Iron and 7.7 % of Nickel while the melted zone exhibited about 65.2 % of Iron and 11.2 % of Nickel so agreeing with SS316L composition of filler-wire.

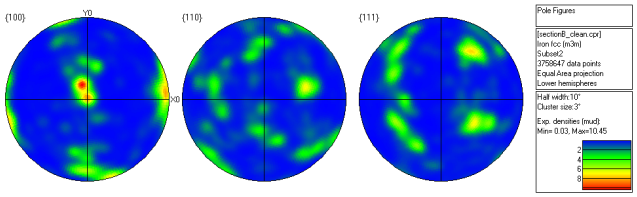

Fig. 6. Pole figures of deposited zone investigated by EBSD technique. The investigated zone is located in the last deposit so near the tip of the deposited zone.

3 Strain-stress measurement with neutron diffraction technique

3.1 The SALSA diffractometer

Neutron diffraction measurements were carried out on SALSA beam line (Strain Analyser for Large and Small scale engineering Applications). SALSA is the dedicated engineering diffractometer of the Institute Max Von Laue Paul Langevin, Grenoble (France). SALSA beam line delivers a monochromatic high neutron flux beam in the range 0.13 nm to 0.34 nm. Furthermore, a two dimensional Positive Sensor Detector (PSD) allows short acquisition time. It has a large choice of collimators. The table is a hydraulic driven Gough-Stewart platform. It is a robot with six degrees of freedom allowing precise scanning of large specimens. The positioning accuracy of the specimen is about 10 μm and it is performed with 3D closed TV-circuit system [10].

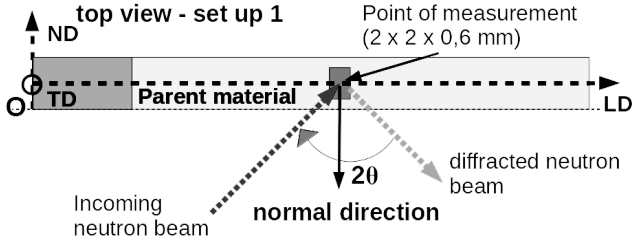

Fig. 7. Set up for measuring the normal strain.

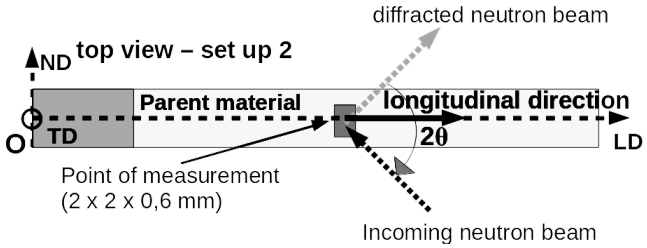

Fig. 8. Set up for measuring the longitudinal strain.

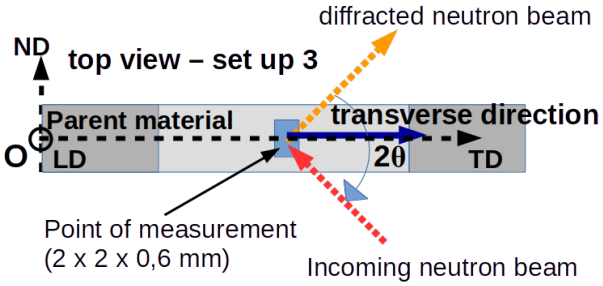

Fig. 9. Set up for measuring the transverse strain. The specimen is rotated of -90° around the ND axis.

A full diffraction pattern was measured along three lines as shown in Figure 1 for the 1-layer specimen. Only one line was scanned with the strain-free specimen (V55) with 1-layer. Specimens with 2, 3 and 5 layers were also only scanned along V55. The neutron settings are reported in Table 3. Each point of measure was made along three directions: the longitudinal direction (LD), the transverse direction (TD) and the normal direction (ND). It is assumed to be the principal directions of

Table 3. Neutron diffraction settings for strain measurements (GV means Gage Volume in mm^3).

Crystal plane	Wavelength	2θ angle	GV-LD	GV-TD	GV-ND
Fe-311	1.66 $\AA$	98.502 °	2x2x0.6	0.6x2x2	2x2x0.6

the stress tensor. The normal and longitudinal directions were measured without unmounting the specimen but it required a rotation of the platform. The sample had to be unmounted and rotated according to axis (O, ND) in order to measure the transverse direction. The experimental set-up for the neutron diffraction measurements are shown in Figures 7, 8 and 9.

The unstrained lattice parameter (d_0), thus θ_0, was determined from a strain-free specimen. This specimen was cut using a water jet cutting machine. The strain-free specimen was available only for the 1-layer specimen. This allowed the measure of θ_0 into the parent material and deposited layer along line V55.

3.2 From neutron diffraction to stress components

The measurement of residual stresses by neutron diffraction is based on Bragg's law [11]:

$$\lambda = 2d_{hkl}\sin\theta_{hkl} \tag{1}$$

where λ is the wavelength of the neutron beam, d_{hkl} is the lattice spacing of atomic planes characterized with Miller indices $\{hkl\}$ and θ_{hkl} is the measured scattering angle. For monochromatic beam diffraction, the wavelength is fixed, its magnitude is known and the measurement of θ_{hkl} gives the lattice spacing. The micro-strain is then computed from the change in the interplanar spacing of the material according to the unstressed state as follows [12, 13] :

$$\varepsilon_i = \frac{d_i - d^0_{hkl}}{d^0_{hkl}} = \frac{sin\theta^0_{hkl}}{sin\theta^i_{hkl}} - 1 \tag{2}$$

Another relation between the micro-strain and the diffracted angle θ_{hkl} can be obtained by differentiating Bragg's law. This second relation is true if the neutron beam is monochromatic [11]:

$$\varepsilon_i = -cot\theta^0_{hkl}.(\theta^i_{hkl} - \theta^0_{hkl}) \tag{3}$$

It is assumed that the principal direction are similar to the deposited layer, that is to say: the longitudinal direction (LD) is parallel to the deposited layer, the transverse direction (TD) is along the vertical axis and the normal direction (ND) is through the thickness of the parent material. The measurements of diffracted angles 2θ were performed in the three directions : LD, TD and ND. Moreover, the measures were located on the median plane of the specimen to ensure that the gage volume was totally filled by the material. Once the three principal micro-strains are measured, the stress, for each direction, is deduced using Hooke's law as follows:

$$\sigma_i = \frac{E}{1+\nu}\varepsilon_i + \frac{\nu E}{(1+\nu)(1-2\nu)}\sum_{i=1}^{3}\varepsilon_i \tag{4}$$

where E is the elastic modulus and ν is Poisson's ratio. Crystallographic moduli relevant to the considered single planes (i.e. Fe-311) are required for monochromatic instruments. The macroscopic and crystallographic values of E and ν used in this study were: E = 182 GPa, ν = 0.307 [14]. The computation of the stress requires the knowledge of the reference diffracted angles θ^0_{hkl}. There are numerous approaches for determining a representative strain-free reference [11, 12, 15]. Two approaches have been investigated in this work:

- strain-free reference cubes or combs from the specimen;
- application of plane stress condition perpendicularly to a given free surface.

These two approaches are presented and compared in the next sections. The first approach is recommended as it is the most reliable but it requires two specimens and so twice measurement time.

3.3 Measured diffracted angles 2θ in the two 1-layer specimens

The strain-free 1-layer specimen is shown in Figure 10. The strain-free specimen (comb-like) was cut with a water jet cutting machine. The three reference angles θ_0 were measured along the black line close to the tip of the comb's teeth (section V55), see Figure 10.

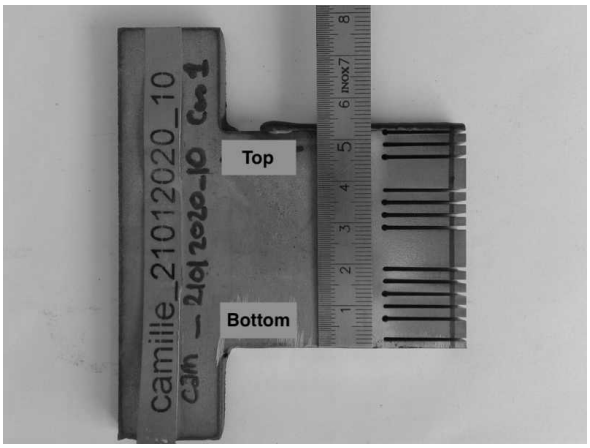

Fig. 10. Strain-free specimen with 1-layer used for obtaining the reference θ_0 parameter. The neutron measurements were performed inside the teeth's comb along the vertical black line where the material is assumed to be strain-free.

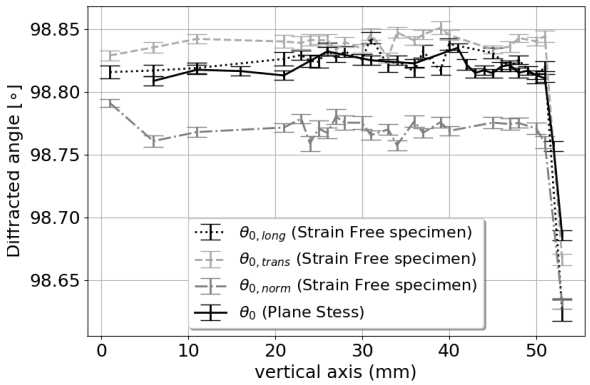

Fig. 11. Evolution of the three reference diffracted angles θ_0 measured along the black line (V55) of strain-free specimen presented in Figure 10. The fourth θ_0 comes from the plane stress assumption. This assumption led to only one reference θ_0 angle. This unique reference θ_0 is computed from a combination of the measured diffracted angles presented in Figure 12.

The three reference angles θ_0 obtained from the strain-free specimen are presented in Figure 11. As it can be seen, the three angles θ_0 are almost constant through the parent material. The average values are 98.77 °, 98.83 ° and 98.84 ° respectively for θ^0_{ND}, θ^0_{LD} and θ^0_{TD}. These constant values confirmed the strain-free state of the reference specimen. The θ_0 values in the deposited layer are different from the ones in the parent material as the deposited material is in SS316L while the parent material is in SS304L.

Figure 12 presents the three diffracted angles θ measured into the 1-layer specimen shown in Figure 2. The behavior of θ angles in the normal and transverse directions are quite similar and slightly varying around their averaged reference values. The θ angle measured in the longitudinal direction was importantly modified. The θ_{LD} is equal to 98.70 ° at z = 0 mm (bottom parent material) to reach a maximum value of 98.95 ° at z = 30 mm and decreased to 98.58 ° in the deposited layer at z = 54 mm. An increase of θ_{LD} in comparison to its reference θ^0_{LD} results in a compressive state while a lower value for θ_{LD} (according to θ^0_{LD}) means a tensile state.

3.4 Calculation of stress with θ_0 obtained from strain-free specimen

Firstly, the three micro-strains are computed from the measured diffracted angles θ as defined by equation 2 using the reference angles θ_0 from the strain-free specimen. The micro-strains ε_{LD} (black dashed line), ε_{TD} (grey line) and ε_{ND} (silver dashed dotted line) are reported in Figure 13. The normal and transverse micro-strains are similar and their values are

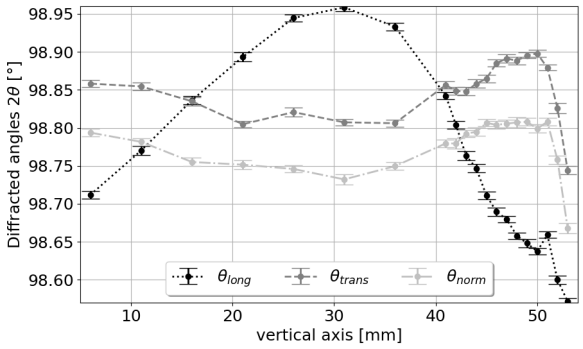

Fig. 12. Diffracted angles along scan line V55 for 1-layer specimen displayed in Figure 2.

fluctuating near 0 . Let's remark that their maximum values are reached close and inside the deposit ($47 \leq z \leq 53$ mm) with -500x10^{-6}. The three stress components are deduced from the measured micro-strains using Hooke's law according to equation 4. The three principal stresses are presented in Figure 14.

The transverse and normal stresses are displayed in Figure 14. They have globally the same trend. Furthermore, these transverse and normal stress profiles are fluctuating around 0 MPa except for the value at the parent material - deposit interface ($z \approx 53$ mm). Conversely, the longitudinal stress profile (black dashed line) varies notably from bottom parent material (z = 0 mm) to the deposited layer ($z \approx 53$ mm). These values varied from 155 MPa at z = 5 mm to a minimum value of -167.1 MPa between z = 26 mm and z = 36 mm and reached a maximum value of 257.9 MPa below the parent material - 1st layer interface. The longitudinal stress dropped in the 1st layer to approximately 12 MPa.

3.5 Calculation of stresses under plane stress condition

In this section, a second method was used for obtaining the reference angle θ_0 required for getting the micro-strains. Then the stress profiles resulting from this second approach are compared to the first approach where a strain-free specimen was used to obtain θ_0. Thus, let's assume that the normal stress is null: $\sigma_{ND} = 0$. This condition is written as follows:

$$\sigma_{ND} = \frac{E}{1+\nu}[\varepsilon_{ND} + \frac{\nu}{1-2\nu}(\varepsilon_{LD} + \varepsilon_{ND} + \varepsilon_{TD})] = 0 \tag{5}$$

It comes for ε_{ND}:

$$\varepsilon_{ND} = \frac{-\nu}{1-\nu}(\varepsilon_{LD} + \varepsilon_{TD}) \tag{6}$$

Finally, by introducing equation 3 into equation 6 and solving it, we obtain the mathematical expression of θ_0:

$$\theta_0 = \frac{1-2\nu}{1+\nu}[\theta_{ND} + \frac{\nu}{(1-2\nu)}(\theta_{LD} + \theta_{ND} + \theta_{TD})] \tag{7}$$

Let's notice that one unique θ_0 is available with the plane stress approach. Furthermore the reference angle θ_0 is determined from the measurement carried out on the 1-layer specimen presented in Figure 12.

Then, the micro-strains are computed according to equation 2 with the same θ_0 for each principal direction. The calculated longitudinal, transverse and normal micro-strains are plotted in Figure 13. Whatever the approach employed for calculating the longitudinal micro-strains, with strain-free specimen or under plane stress, the two profiles are very similar. The transverse and normal micro-strains behave similarly to the one obtained with the strain-free specimen but the transverse is shifted up by 350x10^{-6} while the normal strain is shifted down by -180x10^{-6}. They are not matching anymore nor fluctuating around 0. The computed reference angle θ_0 under plane stress is reported in Figure 11 with the full black line. It can be clearly seen that the unique θ_0 is located in between the transverse and normal reference angles but quite close to the longitudinal reference angle. The values of the unique θ_0 are quite different in comparison to the reference transverse and normal angles measured with the strain-free specimen. This is probably the reason of the shift in these two micro-strains as it is seen in Figure 13. The shifts in the transverse and normal micro-strains are consequently reported on the longitudinal

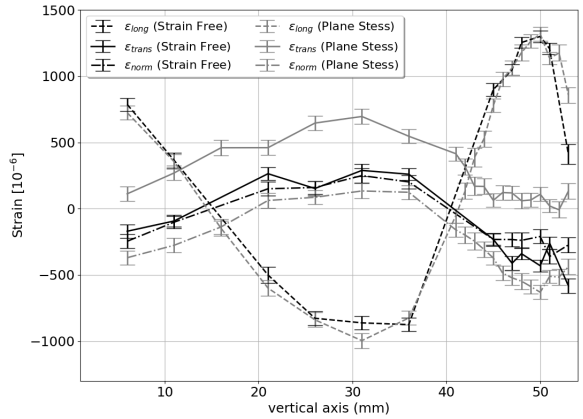

Fig. 13. Calculated micro-strains with reference angle θ_0 measured from strain-free specimen (ε_{LD} is the black dashed line, ε_{TD} is the solid black line and ε_{ND} is the black dashed dotted line). The micro-strains computed under to plane stress assumption are represented with the grey lines. As the plane stress assumption leads to only one reference angle θ_0, the transverse strain ε_{TD} is shifted up.

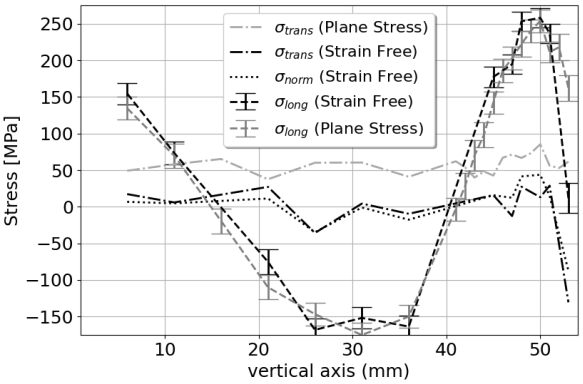

Fig. 14. Calculated longitudinal and transverse stresses under plane stress assumption and comparison to the solution obtained with the strain-free specimen. The stresses computed with strain free specimen are in black colour while the one computed under plane stress are in grey. σ_{LD} is the black dashed line, σ_{TD} is the dashed dotted black line and σ_{ND} is the black dotted line.

and transverse stress values. This shift was assumed to be more or less constant over the scanning line V55. So we checked that the integral of longitudinal stress (or force balance) over section V55 was equal to zero to determine the average shift K_σ.

$$\int_0^{53mm} (\sigma_{long} - K_\sigma) e dz = 0 \tag{8}$$

with e is the parent material thickness and dz is an infinitesimal length in the transverse direction. The balance condition expressed by equation 8 required a constant value of -17 MPa to be verified. The corrected longitudinal and transverse stresses are displayed in Figure 14. After this correction, the two longitudinal stresses matched as it can be seen in Table 4. The maximum longitudinal stress of 257.9 $\pm$ 13.4 MPa is still located just below the interface of the parent material and the layer, at z = 50 mm. In the heat affected zone, the longitudinal stresses computed under plane stress are extremely similar with a maximum stress of 253.7 $\pm$ 15.5 MPa. The stress gradient is around 25 MPa / mm between z = 40 mm and z = 50 mm. In the fuzed zone, the stress value obtained with strain-free specimen is about 11.8 MPa while the one computed with the plane stress approach is around 162.2 MPa probably overestimated. This is likely due to the textured micro-structure, see Figure 4, that has affected the diffraction angles. Furthermore, the plane stress assumption provides a unique θ_0 based on a combination of the three diffracted angles (θ_{LD}, θ_{TD}, θ_{ND}) measured in the fusion zone. The plane stress assumption combined to force balance can be used for computing the stresses when no strain-free specimen is available. No strain-free specimens were available for specimens with 2, 3 and 5 layers. Consequently, the plane stress approach is used to obtain a

Table 4. Longitudinal stress values (in MPa) computed with two approaches for the 1-layer specimen.

TD axis (mm)	6	11	26	31	36	45	47	50	51	53
θ_0 Assumption										
Strain-free (MPa)	154.5	73.6	-168.1	-151.7	-163.5	177.1	194.6	257.9	236.9	11.8
Plane stress (MPa)	134.4	69.8	-146.6	-175.1	-149.9	142.2	202.7	253.7	211.2	162.2

unique reference θ_0 that allows computing the micro-strains and then the stresses. In the fusion zone, this approach led to an overestimated value. It was observed that the diffraction signals in the transverse and normal directions were weak in the melted zone (layers) likely due to the textured micro-structure. This behavior was more pronounced with specimens with 3 layers and more.

Table 5. Correction added to the residual stress profiles computed under plane stress assumption.

specimen	1-layer	2-layers	3-layers	5-layers
K_σ (MPa)	-17	-25	-31	-32

3.6 Effect of layer addition on residual stresses

Let's remember that each deposited layer has a length of about 100 mm. The deposition strategy was such that the end of the first layer is the starting point of the next one and so on until the 5^{th} deposited layer. An interlayer time between each deposit was set to 35 s. Except the 1-layer specimen, the 3 other specimens were scanned along one line (V55) with neutron beam. A strain-free specimen was only available for the 1-layer specimen. The stress values for the 3 specimens with 2, 3 and 5 layers were calculated by applying the plane stress combined to force balance condition as stated in equation 8. The constants K_σ used for balancing the stress in section V55 for each studied specimen are reported in Table 5. Let's remark that an average value of -17 MPa was used for section V55 as well as for the sections V25 and V85 of the 1-layer specimen. The longitudinal stress profiles for the 4 specimens are reported in Figure 15 along section V55. There is no much discrepancies between the four stress profiles in the parent material between 10 mm $\leq$ z $\leq$ 36 mm. Above z = 36 mm, three observations can be done:

- Firstly, the peak of the longitudinal stress shifted from z = 50 mm (1-layer) to z = 55 mm (5-layers). In addition, the magnitude of the longitudinal stress peak decreased from 253.7 $\pm$ 7.8 to 173.7 $\pm$ 5.8 MPa after the deposition of the 2^{nd} layer. This peaks increased to 234.6 $\pm$ 5.3 MPa after the 3^{rd} layer. After the 5^{th}, the maximum longitudinal stress value stabilized to 199.3 $\pm$ 8.8 MPa (at z $\approx$ 55 mm).
- Secondly, the compressive stress zone, inside the parent material, increased with the addition of layers, by about 5 mm and the minimum longitudinal stress values slightly moved up from -175.1 MPa to -148.9 MPa. A stress plateau, with values ranging between -130 to -140 MPa, is clearly visible with the 5-layers specimen.
- Lastly, the longitudinal stress values measured in the last deposited layer tends to decrease from 137.3 $\pm$ 5.4 MPa (1-layer) to 112.4 $\pm$ 21.4 MPa (3-layers) and then 57.7 $\pm$ 52 MPa for the 5-layers specimen.

The decrease of longitudinal stress in the melted zone has been already observed in similar additive manufactured parts [16]. As the number of layer increased, the uncertainties on the stress values in the fusion zone increased, especially with the 3-layers and 5-layers specimens. This is also likely due to the large size of columnar grains. Indeed the gage volume is located in the middle of the specimen where the size of columnar grains is up to few millimeters. The gage volume was possibly filled in with one or two grains so the measure was done probably at the grain level.

4 Discussions

4.1 Effect of the reference angle θ_0

The longitudinal, transverse and normal stresses were calculated using two methods: the first method used a strain-free specimen for getting the three reference diffracted angles θ_0 while the second method consisted in applying the plane stress assumption on the normal stress. This second method led to an unique reference diffracted angle θ_0 (calculated from the

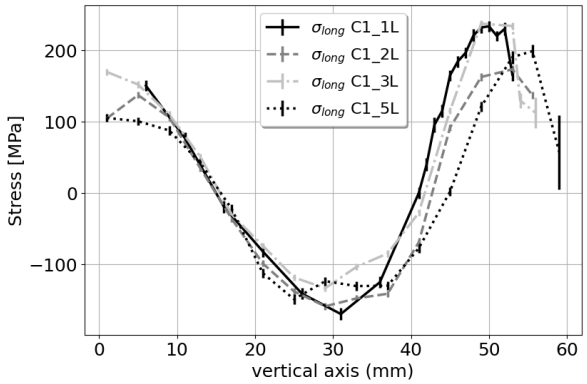

Fig. 15. Longitudinal stresses calculated under the plane stress assumption (σ_{ND} = 0) for specimens with 1, 2, 3 and 5 layers (along line V55).

measured diffracted angles displayed in Figure 12). This unique reference angle θ_0 is reported in Figure 11. The first method implies measuring two specimens so it requires twice experimental time.

The longitudinal stresses calculated under plane stress assumption exhibited a shift in comparison with the one calculated with the strain-free specimen. The longitudinal stress profile calculated with θ_0 from the strain-free specimen was well balanced whereas the one computed under plane stress was shifted and so unbalanced. A constant value was added to the longitudinal stress values in sort of the force balance was verified. These constant values are reported in Table 5. These values varied between -17 MPa and -32 MPa. The uncertainties on the longitudinal stress profiles were estimated between 4.8 and 9.4 MPa. This drift is up to 3 times higher than the uncertainty. Thus the plane stress assumption combined to force balance condition can be consistently applied on the studied specimens.

The main difference between the two calculated longitudinal profiles resided in the melted zone (or deposited layer). This value is close to zero when using the strain-free specimen while it is 162 MPa under plane stress assumption as reported in Figure 14 and in Table 4. The measure was made at z = 53 mm, so the interface between the parent material and the deposited layer. The parent material was partially melted and diluted with the SS316L filler-wire. The strain-free specimen and the 1-layer specimen were built with the same process parameters. Even if the two specimens were built under the same conditions, a small change in the dilution may have resulted in different diffracted angle θ_0, especially with the second method (as the specimen is not strain-free). Indeed, the use of strain-free specimen gives likely better results in such zone where dissimilar materials are melted together. The reference crystal lattice parameter d_0 (or reference diffracted angle θ_0) is very sensitive to local chemical composition.

4.2 Stress field in 1-layer specimen

Longitudinal stress profiles at the three sections V25, V55 and V85 are displayed in Figure 16. The longitudinal stress profiles at the three sections are quite close except for the stress value of section V25 located at z = 53 mm. These sections were subjected to similar deposition cycles (thermal steady state). Thermocouples 3 and 4 were respectively located close to sections V55 and V85 and they are located 5 mm under the deposition surface as shown in Figure 1. These two thermocouples have experienced the same thermal loading, with a delay, as it is reported in Figure 3 for the 5-layers specimen.

The maximum longitudinal stress value is localized 3 mm under the deposition surface for the three sections. Coules et al investigated the in-situ plastic strain generation during a GTAW experiment [17]. They stated that the material developed plastic strain around the melted zone and up to 20 mm where the temperature gradient are the highest and thus the thermal compression.

According to Figure 3, the thermal gradient in section V55 is about 159 K/mm as thermocouples 2 and 3 are located in this section respectively 3 mm and 5 mm under the deposition surface. They reached the respective temperature peaks of 1188 K and 869 K during the deposition of the 1^{st} layer. This zone was subjected to strong compression due to the thermal expansion during the heating against the stiff and globally cold parent material. During the solidification and cooling, this zone contracted thermally until the ambient temperature was reached as it is schematized in Figure 17. It led to tensile stress values, around 220-260 MPa as shown in Table 6, just below the value of 287 MPa which is the yield stress of the Stainless Steel 316L [18]. It is quite common, in arc welding, to measure residual stresses close to the yield stress of the studied material [19]. The drop of longitudinal stress in the deposited layer is probably due to the parent material bending as the displacement of its free-end moved upward of 0.45 mm after getting back to the ambient temperature [20].

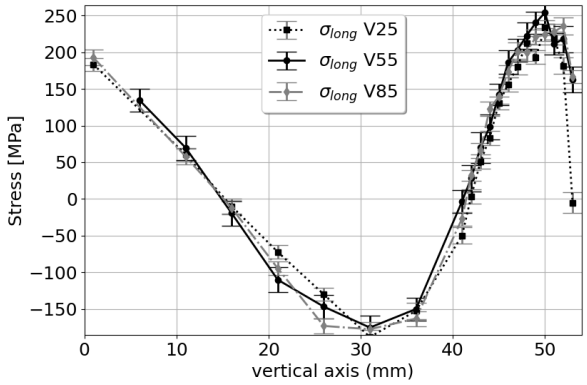

Fig. 16. Longitudinal stresses along lines V25, V55 and V85 of the 1-layer specimen. The longitudinal stresses were computed under plane stress assumption.

Table 6. Longitudinal stress values (in MPa) in the heat affected and melted zones at the 3 sections V25, V55 and V85 of 1-layer specimen (computed under plane stress assumption).

TD axis (mm)	45	47	50	51	53
V25 (MPa)	130.6 ± 4.2	179.8 ± 5.3	233.2 ± 5.2	218.7 ± 4.4	-5.1 ± 6.9
V55 (MPa)	142.2 ± 7.5	202.7 ± 7.8	253.7 ± 7.7	211.2 ± 7.1	162.2 ± 8.7
V85 (MPa)	139.5 ± 4.8	201.1 ± 6.2	223.6 ± 4.5	227.6 ± 5.3	166.3 ± 4.4

4.3 Effect of layer addition on the residual stresses

For additive manufactured components, the residual stresses in the building direction are significant compared to classic butt-welded specimens. This is a result of the layer-by-layer re-heating and re-cooling process, where the thermal gradient during metal solidification develops oppositely to the building direction.

It is well known that tensile residual stress occurs in the weld bead (or deposit) due to the contraction of the molten zone during the solidification constrained by the surrounding solid metal. The compressive stress generated inside the parent material is a consequence of the high heating that generated high temperature gradient from the top parent material to its centre and so an important thermal compression inside. The longitudinal stress is tensile in the bottom part of the parent material as it bent slightly upward due to the material contraction in both HAZ and FZ. The observed experimental behaviour is presented in Figure 17. As a matter of fact, the experiment was designed such as the parent material is free to deform at one extremity while the other is clamped in order to behave like a cantilever beam. The vertical displacement of the parent material free-end was monitored with a laser system. The maximum displacement was about 0.45 mm for the 5-layers specimen after cooling down to ambient temperature (300 K) [20]. The highest longitudinal stresses occurred between 3

Table 7. Longitudinal stresses (in MPa) in the heat affected and fusion zones for all investigated specimens (computed under plane stress assumption).

TD axis (mm)	41	45	49	53	55	59
1-layer (MPa)	-3.2 ± 7.7	142.2 ± 7.5	240 ± 7.6	162.3 ± 8.7	-	-
2-layers (MPa)	-69.9 ± 4.2	91.9 ± 4.7	163 ± 5.3	173 ± 5.8	137.3 ± 5.4	-
3-layers (MPa)	-27.4 ± 4.5	115.5 ± 4.5	237.9 ± 4.6	234.6 ± 5.3	112.4 ± 21.5	-
5-layers (MPa)	-77.2 ± 6.6	1.9 ± 5.8	121.4 ± 6.7	190.8 ± 9	199.3 ± 8.8	57.7 ± 52

and 4 mm below the interface of parent material – 1^{st} layer where the parent material undergone important plastic work.

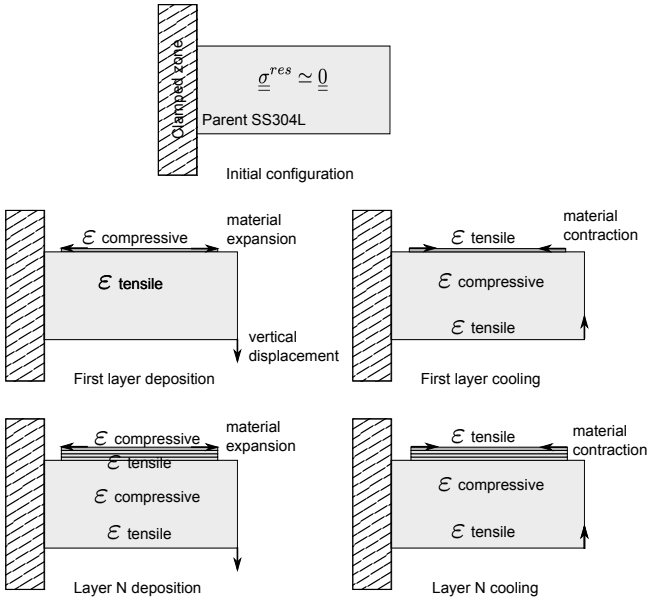

Fig. 17. Schematisation of the generation of the micro-strains and stresses in the specimen layer after layer. Top: initial micro-strains and stresses in the specimen before the deposition of the first layer. Middle: generation of micro-strains and stresses during the deposition of first layer. Bottom: generation of micro-strains and stresses during the deposition of the next layer.

The position of this maximum longitudinal stress shifted to the parent material - 1^{st} layer interface after the 2^{nd} layer. The longitudinal stress profile showed another shift of the maximum stress in the 1^{st} layer after the deposition of the 5^{th} layer. This maximum longitudinal stress decreased from 257.7 $\pm$ 7.7 MPa (at z = 50 mm), after the 1^{st} layer, to 199.3 $\pm$ 8.8 MPa (at z = 55 mm) after the deposition of the 5^{th} layer, see Table 7, up to 20 % of stress decrease. Some stress relaxation likely occurred after the 4^{th} or 5^{th} depositions. The longitudinal stress increased after the 3^{rd} deposition and reached values similar to the 1^{st} deposition. The layers 1, 3 and 5 were deposited in the same direction while 2 and 4 were done in the opposite direction (but data for the 4^{th} are not available). The even layers were done in direction of the clamping system: the vice. The presence of the vice may have limited some thermal dilatation at the end of the deposited layer what likely reduced the tensile longitudinal stresses. Stress relieving temperature starts around 700 K for steels and it requires few hours to allow stress relief [21]. For temperature as high as 1350 K, stress relieving reached 90 % for times as short as 5 minutes [22] for AM parts made with selective laser melting process. According to the measured temperature in Figure 3, the temperature of the parent material remained beyond 700 K above z = 48 mm since the deposition of the 3^{rd} layer. The maximum temperature reached during the 3^{rd} layer at Tc2 appeared at 115 s and it remained between 1000 K and 700 K for about 160 s. This means that the material above thermocouple Tc2 remained likely above 1000 K for times longer than 160 s. From a previous thermo-mechanical study [20], the material above Tc2, so for Z $>$ 50 mm , experienced temperatures up to 1300 – 1400 K during the deposition of 3^{rd} layer and above 1000 K during the deposition of the 5^{th} layer. These high temperatures associated to sufficient soaking time, at least 160s, may have produced a local stress relaxation. Inside the deposited layers, a decrease of longitudinal stress is measured. A drop in the longitudinal stress in the deposited layers is often observed in WAAM parts after unclamping [5] due to mechanical balance. In this work, the parent material was free to deform. This decrease of longitudinal stress in added layers is probably due to some stress relaxation as the temperature of layers 1, 2 and 3 were globally varying between 1000 K and 1400 K during the deposition of the 4^{th} and 5^{th} layers.

5 Conclusions

This research work presented the residual stress field in four specimens. These specimens consisted of a parent material in Stainless Steel 304 with up to five deposits stacked vertically. The first part of this work is dedicated to the choice of the method for obtaining the reference diffracted angle θ_0. θ_0 is required for calculating the micro-strains and thus the stresses. The best practice is to work with a strain-free specimen in order to get three reference diffracted angles. Such strain-free specimen was available for one out of the four specimens. A second approach was used for obtaining the reference diffracted angle θ_0 by applying the plane stress assumption. These two approaches are compared and discussed. In the second part, the plane stress assumption was applied to the three other specimens in order to evaluate the effect of layer addition on the residual stresses.

It can be stated about the two approaches used for obtaining the reference angle θ_0:

- The use of strain-free specimen is of course the best method to get the reference diffracted angle θ_0 as it gives three reference angles, one for each principal direction.
- The plane stress assumption is only able to provide one unique reference angle θ_0. The unique θ_0 produced some offset in the computation of the micro-strains and it led to an unbalanced stress field. The use of force balance on the stress field can resolve this offset matter. The offset was evaluated between -17 and -32 MPa according to the investigated specimens.
- Finally, the two methods led to close longitudinal stress profiles. A slight difference is visible on the transverse stress profiles: the one obtained with the strain-free specimen is almost null while the second one remained slightly shifted.

The measured residual stresses in the four specimens, according to the plane stress assumption, showed that:

- The residual stresses were measured along three different scanning lines in the 1-layer specimen. These scanning lines were spaced of 30 mm and were localized in thermal steady state according to the temperature recordings. The residual stresses are extremely similar along these three lines confirming that they undergone the same thermal loadings.
- The longitudinal stress is divided in three main zones: tensile at the bottom of the parent material with values between 100 and 180 MPa below the yield stress of SS304L parent material; A large compressive zone inside the parent material with a minimum value close to -170 MPa; Another tensile zone localized around the deposition zone where the thermal loadings occurred. The maximum longitudinal stress value reached 250 to 260 MPa. Some neutron measurements showed that the tensile longitudinal stresses decreased as the number of layers increased. The longitudinal stress became compressive after the deposition of the 5^{th} layer.
- For all the specimens, the maximum longitudinal stress value is located at the interface of the parent material and 1^{st} layer. This maximum value moved inside the 1^{st} layer after the deposition of the 4^{th} and 5^{th} layers. The maximum longitudinal stress was about 257 MPa after the deposition of the 1^{st} layer and it ended to 199 MPa after the 5^{th} layer.
- The five thermal cycles due to the deposition of each layer likely produced some stress relieving. A decrease of the maximum longitudinal stress is observed after the 2^{nd} layer. After the deposition of the 5^{th} layer, this maximum longitudinal stress was 20 % lower than the one observed for the 1^{st} layer.
- The longitudinal stress was affected after each thermal loading due to a new deposited layer. This effect is visible up to 10 - 12 mm below the interface between the parent material and 1^{st} layer (located at z = 53 mm) and in the previous deposited layer. After the 3^{rd} deposition, the initial temperature of the deposition zone remained over 700 K according to the thermocouples located at z = 50 and z = 48 mm (so about 9 to 11 mm below the deposition zone). This temperature was probably close to 1300 K according to a numerical study [23]. Furthermore, after the 3^{rd} deposition, the thermocouples showed a stabilization of the initial temperature of the deposition zone. The stress relieving probably occurred after the 3^{rd} layer despite very short soaking times inferior to 3 min.
- The longitudinal tensile zone at the bottom of the parent material is assumed to be a consequence of the slight bending upward after each deposition cycles [20]. It is also combined to a stress balance due to the high tensile stresses in the deposition zone and the large compressive stresses inside the parent material.

References

[1] Jin, W., Zhang, C., Jin, S., Tian, Y., Wellmann, D., and Liu, W., 2020. "Wire arc additive manufacturing of stainless steels: A review". *Applied Sciences (Switzerland),* **10**(5).

[2] Ding, D., Pan, Z., Cuiuri, D., and Li, H., 2015. "A multi-bead overlapping model for robotic wire and arc additive manufacturing (WAAM)". *Robotics and Computer-Integrated Manufacturing,* **31**, pp. 101–110.

[3] Martina, F., Mehnen, J., Williams, S., Colegrove, P., and Wang, F., 2012. "Investigation of the benefits of plasma deposition for the additive layer manufacture of Ti-6Al-4V". *Journal of Materials Processing Technology,* **212**(6), pp. 1377–1386.

[4] Syed, W., Pinkerton, A., and Li, L., 2005. "A comparative study of wire feeding and powder feeding in direct diode laser deposition for rapid prototyping". *Applied Surface Science,* **247**, pp. 268–276.

[5] Ding, J., Colegrove, P., Mehnen, J., Ganguly, S., Sequeira, P. A., Wang, F., and Williams, S., 2011. "Thermo-mechanical analysis of Wire and Arc Additive Layer Manufacturing process on large multi-layer parts". *Computational Materials Science,* **50**(12), pp. 3315–3322.

[6] Colegrove, P., Ikeagu, C., Thistlethwaite, A., Williams, S., Nagy, T., Suder, W., Steuwer, A., and Pirling, T., 2009. "Welding process impact on residual stress and distortion". *Science and Technology of Welding and Joining,* **14**(8), pp. 717–725.

[7] Allen, W., Andreani, C., Hutchings, M., and Windsor, C., 1985. "Neutron diffraction methods for the study of residual stress fields". *Advances in Physics,* **34**, pp. 445–473.

[8] Fitzpatrick, M., and Lodini, A., 2003. *Analysis of Residual Stress by Diffraction using Neutron and Synchrotron Radiation*. Taylor and Francis.

[9] Pratihar, S., Turski, M., Edwards, L., and Bouchard, P., 2009. "Neutron diffraction residual stress measurements in

a 316L stainless steel bead-on-plate weld specimen". *International Journal of Pressure Vessels and Piping,* **86**(1), pp. 13–19.

[10] Pirling, T., Bruno, G., and Withers, P., 2006. "SALSA-A new instrument for strain imaging in engineering materials and components". *Materials Science and Engineering A,* **437**(1), pp. 139–144.

[11] Hutchings, M., Withers, P., Holden, T., and Lorentzen, T., 2005. *Introduction to the Characterization of Residual Stress by Neutron Diffraction*. Taylor and Francis.

[12] Krawitz, A., and Winholtz, R., 1994. "Use of position-dependent stress-free standards for diffraction stress measurements". *Materials Science and Engineering A*.

[13] Ohms, C., Wimpory, R., Katsareas, D., and Youtsos, A., 2009. "NET TG1: Residual stress assessment by neutron diffraction and finite element modeling on a single bead weld on a steel plate". *International Journal of Pressure Vessels and Piping,* **86**(1), pp. 63–72.

[14] Ledbetter, H., 1977. Elastic properties of zinc: A compilation and a review.

[15] Withers, P., Preuss, M., Steuwer, A., and Pang, J., 2007. "Methods for obtaining the strain-free lattice parameter when using diffraction to determine residual stress". *Journal of Applied Crystallography,* **40**(5), pp. 891–904.

[16] Hönnige, J., Williams, S., and Roy, M., 2017. "Residual Stress Characterization and Control in the Additive Manufacture of Large Scale Metal Structures". *Residual Stresses 2016,* **2**(July), pp. 455–460.

[17] Coules, H., Colegrove, P., Cozzolino, L., and Wen, S., 2012. "Experimental measurement of biaxial thermal stress fields caused by arc welding". *Journal of Material Processing Technology,* **212**, pp. 962–968.

[18] Depradeux, L., 2004. "Simulation numérique du soudage - Acier 316L Validation sur cas tests de complexité". *Simulation*, pp. 2004–2004.

[19] Macdonald, K., 2016. *Fracture and Fatigue of Welded Joints and Structures*. Woodhead Publishing Series in Welding and Other Joining Technologies. Elsevier Science.

[20] Cambon, C., Bendaoud, I., Rouquette, S., and Soulié, F., 2022. "A waam benchmark: From process parameters to thermal effects on weld pool shape, microstructure and residual stresses". *Materials Today Communications,* **33**, p. 104235.

[21] Kou, S., 2003. *Welding metallurgy, 2nd ed.* Wiley-Interscience.

[22] Chao, Q., Thomas, S., Birbilis, N., Cizek, P., Hodgson, P., and Fabijanic, D., 2021. "The effect of post-processing heat treatment on the microstructure, residual stress and mechanical properties of selective laser melted 316l stainless steel". *Materials Science and Engineering A: Structural Materials: Properties, Microstructure and Processing,* **821**, July.

[23] Cambon, C., Rouquette, S., Bendaoud, I., Bordreuil, C., Wimpory, R., and Soulié, F., 2020. "Thermo-mechanical simulation of overlaid layers made with wire + arc additive manufacturing and GMAW-cold metal transfer". *Welding in the World,* **64**(8), pp. 1427–1435.